Energy, Mines and Resources Canada
Énergie, Mines et Ressources Canada

CANMET
Canada Centre for Mineral and Energy Technology
Centre canadien de la technologie des minéraux et de l'énergie

# ANALYSIS OF DEPOSITS, SCALES AND SUB-SCALES ON ALLOYS EXPOSED IN THE POINT TUPPER ATMOSPHERIC FLUIDIZED BED COMBUSTOR

H. Hindam, R. Packwood and J.B. Gilmour
Corrosion Science and Metal Physics Section

February 1986

PHYSICAL METALLURGY RESEARCH LABORATORIES
REPORT: PMRL 86-11(TR)

PHYSICAL METALLURGY RESEARCH LABORATORIES

REPORT: PMRL 86-11(TR)

# ANALYSIS OF DEPOSITS, SCALES AND SUB-SCALES ON ALLOYS EXPOSED IN THE POINT TUPPER ATMOSPHERIC FLUIDIZED BED COMBUSTOR

by

H. Hindam, R.Packwood and J.B. Gilmour

## ABSTRACT

A wide range of commercial Fe-based alloys (ferritic and austenitic) were exposed in an atmospheric fluidized bed combustor (AFBC) utilizing a S-containing coal and a limestone sorbent. This report describes the morphology and composition of the deposits, scales and sub-scales formed on selected samples of the alloys after up to three 1000 h runs.

LABORATOIRES DE RECHERCHE EN MÉTALLURGIE PHYSIQUE

RAPPORT: PMRL 86-11(TR)

# ANALYSE DES DÉPÔTS, ÉCAILLES ET SOUS ÉCAILLES SUR DES ALLIAGES EXPOSÉS DANS LE COMBUSTEUR AU LIT FLUIDISÉ DE POINT TUPPER.

par

H. Hindam, R.Packwood et J.B. Gilmour

## RÉSUMÉ

Un grand nombre d'alliages commerciaux de Fe (ferritiques et austénitiques) ont été exposés dans un combusteur atmosphériques au lit fluidisé qui est alimenté avec du charbon sulfureux et du calcaire. Ce rapport décrit la morphologie et la composition des dépots, écailles et sous-écailles sur quelques échantillons des alliages après des essais qui ont duré jusqu'à 3000 h.

## INTRODUCTION

The Department of Energy, Mines and Resources and the Nova Scotia Power Corporation have conducted a materials evaluation program to determine the long-term behaviour (up to 10 000 h) of commercial alloys in an AFBC utilizing coal containing up to 4 wt % S and a limestone sorbent. A description of the program, evaluation procedures and results obtained after certain 1000 h runs can be found elsewhere (1-4). This report is confined to analyzing the degradation behaviour of in-bed tubes based primarily on X-ray diffraction (XRD), electron probe micro-analysis (EPMA) and optical microscopy (OM). This analysis was complemented with Auger electron spectroscopy (AES).

The specimens discussed in this report represent only a very minor sample of the almost 800 specimens exposed in the combustor during the program and thus, before conclusions regarding the mechanism of corrosion can be drawn, analysis of samples exposed for longer times and at various temperatures must be carried out. This work is continuing and the results will be reported later.

## PROCEDURES

As described in Ref. (1), 20 machined samples (nominally 50 mm diameter, 40 mm long with a 6-mm wall thickness) were screwed together to form a 800-mm test section in a 2-m long tube. After exposure in the combustor, each tube segment was sectioned into three rings. The central ring was examined with an optical microscope. Based on these observations, typical samples were selected for XRD and EPMA. These analyses were carried out on samples cut from the two other rings.

A list of the selected samples is included in Table 1. Sample labelling is described in the above references. A summary of the experimental conditions (exposure temperatures and times) are also given. The compositions of the various alloys are given in Table 2.

XRD analysis was carried out with a Debye-Scherrer camera on powder samples which were scraped from the rings. However, some expected phases could not be detected by this procedure. To reveal phases undetected by bulk analysis, a few samples were examined with a stereo OM and, based on

color and texture contrasts, small amounts of powders were selectively scraped from the sample and analyzed with a Gandolphi X-ray camera.

Standard metallographic procedures were followed in preparing samples for EPMA. A thin carbon coating was deposited on the samples to minimize electric charging. Point counting, line scanning and mapping techniques were used to characterize the samples fully. The elemental concentrations at a given point were measured pairwise in sequence. The oxygen concentration was found by difference. When analyzing micro-features (precipitates), it must be realized that interference from the surrounding matrix can occur. This possibility is considered when the results are interpreted.

The quantitative EPMA data are reported in the tables accompanying the optical photographs. The features analyzed are referenced by lower case letters in the text, the photograph and the table. Upper case letters refer to specific figures. Compositions are in wt %, and at % values are enclosed in parentheses.

## RESULTS AND DISCUSSION

The observations are presented and discussed in two sections: the first deals with the behaviour of the ferritic alloys (carbon and Cr-Mo steels) and the second is devoted to the behaviour of austenitic alloys (stainless steels and Incoloy 800H). This format was adopted because of some similarity in behaviour among the alloy compositions in each group.

### FERRITIC ALLOYS

Carbon and Cr-Mo steels were included in two types of air-cooled tubes operating at nominal temperature gradients (450-575°C) and (550-700°C). At a given location along the tubes, the temperature was not uniform around the circumference; the top being consistently hotter than the bottom (2).

A few samples, labelled 2A1-, were part of a tube which was exposed in the combustor during the first 1000 h run. This tube was exposed to temperatures higher than in the subsequent runs (2). Lower temperatures were achieved by modifying to the design of the tube core. Examination of samples

from several runs confirmed that, except for an increase in thickness, the nature and microstructure of the corrosion products were not changed by the higher temperature during that first run.

Carbon Steel

Two cross-sections of a carbon steel sample are shown in Fig. 1. Typical specimens exhibited two distinct layers: the outer layer (Fig. 1a) had a grainy, striated structure; whereas the inner layer (Fig. 1b) was dense and usually contained fewer microscopic features.

The results of XRD analyses are presented in Table 3. The following phases were detected: $Fe_3O_4$ (major phase), $Fe_2O_3$ and $CaSO_4$.

EPMA indicated that the outer layer was rich in Ca, Fe and S, and that it contained moderate amounts of Al and Si. Electron probe line scans revealed that this layer was very heterogeneous. Although some correlation existed between the Ca and S contents, there were regions rich in Ca and poor in S. It was, therefore, concluded that both $CaSO_4$ and CaO were present. The Fe content was quite high, the Fe probably being present as $Fe_2O_3$, $Fe_3O_4$ and FeS.

The inner layer consisted mainly of $Fe_3O_4$ and small amounts of FeS in the form of a network (Fig. 1c) decorating the magnetite grain boundaries. Minor amounts of Si, Cr, Mn and Ca could also be detected, although Ca was confined to the region adjacent to the outer layer.

It is evident that the deposition of bed material, which is mainly composed of $CaSO_4$, CaO, $SiO_2$ and $Al_2O_3$ (see Table 4), contributed to the formation of the outer layer, whereas the inner layer is formed by diffusional growth. Therefore, in the following text, the outer and inner layers are referred to as deposit and scale, respectively. The presence of Ca in the outermost region of the scale confirmed that an interaction between the scale and deposit did occur. The relative thickness of the deposit and scale varied around the ring and appeared to depend also on the location in the combustor. On many samples, the deposit layer was absent at the bottom of the tube. This is believed to be the result of erosion by the bed material (2).

T11 AND T22

With the exception of a few features, the deposit and scale on the T11 and T22 alloys exhibited similar morphologies. A cross-section of a typical T22 sample is shown in Fig. 2. An electron image and the corresponding X-ray maps for all the detected elements are included in Fig. 3.

The main elements present in the deposit (Fig. 2a) were Fe, O, Ca, S, Si and Al. The last two elements were not included in the quantitative analysis. However their concentration was estimated as 1-2 wt % based on Energy Dispersive X-ray Spectroscopy (EDXS). The composition of the deposit was quite variable from one location to another. The relative S/Ca ratio was low, indicating that the relative $CaO/CaSO_4$ ratio was high.

The scale (Fig. 2b) consisted of $Fe_3O_4$ containing small amounts of dissolved Cr (~3 wt %) and minor quantities of S, Si, Al and Mo. Small amounts of Ca were present in a thin region close to the deposit/scale interface. This region also contained a bright phase in the form of streaks (Fig. 2c) which were rich in Fe, S, and O. The X-ray map indicated that they were also rich in Si. Most probably, this region consisted of FeS and $SiO_2$. Aluminum and to a lesser extent S and Si tend to be concentrated at the scale/alloy interface.

The scale thickness was non-uniform. In many cases, the thicker regions contained stringers (Fig. 2d) extending throughout the scale and the deposit. The stringers were too thin for analysis without interference from the surrounding matrix. However their composition was probably FeS. These FeS stringers could offer a short-circuit path for the outward transport of Fe ($D_{Fe}$ in FeS >> $D_{Fe}$ in $Fe_3O_4$).

Minor internal precipitation occurred in the alloy to a depth of 10-15 μm. The precipitates (Fig. 2e), which grew preferentially at alloy grain boundaries, appeared to be predominantly composed of $Cr_2O_3$ with a small amount of CrS.

Unlike the T22 alloy, the scale formed on T11 was uniform in thickness. As expected, it contained slightly less chromium.

T91

A cross-section of the top of a T91 ring is shown in Fig. 4. The sample exhibited a deposit (Fig. 4a), a scale (Fig. 4b) and a thin (~10 μm deep), discontinuous band of internal precipitates (Fig. 4e).

The scale was slightly thicker at the locations where internal precipitation had occurred. Deep-etching with a bromine-methanol solution revealed the presence of a thin film (Fig. 4d) at the precipitate-free locations (Fig. 5).

The morphology of the deposit was similar to that found on the T22 alloy. However, the sulfur content of the deposit on T91 was higher than on T22. The increase in the sulfur content was associated with a higher volume fraction of FeS in the form of particles or streaks (Fig. 4c).

The scale was an $(Fe,Cr)_3O_4$ solid solution containing 14 wt % Cr. The internal precipitates and the inner film were probably $Cr_2O_3$ because both were rich in Cr and oxygen. The apparent high concentration of Fe most probably came from the alloy matrix.

The bottom cross-section of the same ring is shown in Fig. 6. No deposit was found in this region. The scale (Fig. 6a) was non-uniform in thickness and its interface undulatory with the alloy as with the T22 sample (Fig. 2). The average scale thickness at the ring bottom was greater than at the top despite the lower average temperature of the bottom (Table 1). A few bright streaks (Fig. 6b) were dispersed in the scale. A thin (~10 μm) band of internal precipitates (Fig. 6c) was present in the alloy.

The scale at the bottom was slightly lower in Cr (~11 wt %) and was richer in Fe (~58 wt %) compared with the scale at the top (~13 wt % Cr, ~53 wt % Fe). Unlike the top, small amounts of S (~0.3 wt %) were detected in the scale. The streaks (Fig. 6b) were too thin for analysis without interference from the surrounding matrix. However, their morphology was very similar to the morphology of the streaks in Fig. 2 and 4 and probably they were of similar composition (FeS). The internal precipitates (Fig. 6c) were composed of $Cr_2O_3$ and CrS.

A prominent feature of many of the T91 samples is the presence of thick, adherent, multi-layered deposits. A cross-section of the top of another T91 ring and the corresponding X-ray maps are included in Fig. 7 to illustrate this observation. The two outer layers (Fig. 7a,b) were considered as a deposit because they were rich in Ca. The outermost layer (Fig. 7a) contained higher amounts of Ca and S and less Fe than the layer beneath it (Fig. 7b). In many instances, the deposit on the T91 alloy exhibited a more complex structure consisting of several non-uniform layers and embedded scale fragments.

The scale (Fig. 7c) and the inner film (Fig. 7d) were of similar compositions to the respective features on the other T91 sample. The inner $Cr_2O_3$ film was not fully protective, because it was penetrated by S. The alloy region contiguous to the film was depleted in Cr.

## AUSTENITIC ALLOYS

Types 304H, 310 and 347H stainless steel were more resistant than the other austenitic alloys included in this program although the first composition was tested in air-cooled tubes only. These alloys exhibited a common degradation pattern with the exception of a few particular features.

The attack on the other alloys (HK40, 253MA and Incoloy 800H) was more severe and the depth of attack varied significantly around the tube. Usually, the bottom of the tube was more severely attacked than the top. In many instances, the degradation behaviour was dependent on the microstructures and compositions of the alloys.

Unless otherwise noted, the following description of the degradation behaviour is based on samples from a tube exposed for 3 000 h at bed temperature (850°C). Segments for EPMA and AES were cut from the bottoms of the rings.

## 304H, 310 AND 347H

A common morphology observed on these stainless steels is illustrated in Fig. 8, for type 310 stainless steel. An electron image and the corresponding X-ray maps are included in Fig. 9.

No deposit was found on this sample. The scale consisted of an inner thin (5 µm) film (Fig. 8c) and an external relatively thick (30 µm) layer (Fig. 8a,b). The inner film is resolved in the X-ray maps and its presence was also confirmed by line scanning across the scale. Two types of precipitates were observed in the alloy: small intrusions (8,d) emanating from the inner film and small globular precipitates (8,e) mainly formed at alloy grain boundaries to a depth of ~50 µm. The advance of the intrusions into the alloy resulted in the entrapment of small alloy particles in the inner region of the scale.

The "inner film" (Fig. 8c) and the small intrusions (Fig. 8d) were probably $Cr_2O_3$. The structure and composition of the rest of the scale were quite complex. The outer region of the scale (Fig. 8a) was unusually rich in Cr and contained some Fe. The inner region (Fig. 8b) consisted of bands, rich in Fe, Ni or both that contained moderate amounts of Cr. Mn was present throughout the scale, but its concentration was higher in the inner region. Very small amounts of S (~0.1 wt %) could be detected at a few locations in the outer region.

By EPMA it was found that the globular precipitates were primarily composed of Mn and S, devoid of Fe and Ni, as indicated by the X-ray maps (Fig. 9). The Fe and Ni contents of these precipitates indicated in the table accompanying Fig. 8 are attributed to interference from the alloy matrix. AES analysis of another 310 sample from the same tube confirmed the presence of Mn, Cr and S only (Fig. 10). The amount of Cr in this Cr-Mn-S solid solution decreased toward the precipitation front. The alloy in the precipitation zone was depleted in Cr from ~24 wt % (bulk concentration) to 16 wt %.

Deposit could be found on a few samples. The cross-section of the top of a 347H ring which exhibited deposit is shown in Fig. 11. The deposit (Fig. 11a), ~50 μm thick, overlaid a thin (10 μm) scale (Fig. 11b,c). Internal precipitation (Fig. 11d) occurred in the alloy but to a very limited extent.

In addition to Ca, S, O and Fe, the deposit contained moderate amounts of Si and Al (undetermined) and small amounts of Mn. Similar to the deposit on the carbon and Cr-Mo steels, the ratio of S to Ca was low; however, the concentration of Fe in the deposit formed on the 310 sample was low.

The scale was probably $Cr_2O_3$ containing ~2 wt % Mn and ~1.5 wt % Fe. The outer edge (Fig. 11b) was relatively rich in Mn (probably in the form of $MnCr_2O_4$). The inner edge (Fig. 11c) contained some S (probably in the form of CrS). The internal precipitates (Fig. 11d) were too small for analysis; however, they were most probably $Cr_2O_3$ because they were rich in Cr and no S could be detected in the precipitation zone.

The cross-section of the bottom of the same ring is included in Fig. 12. Only a trace of a deposit (Fig. 12a) was present. The scale (Fig. 12b,c) was non-uniform in thickness. The morphology of attack was

similar to that observed at the top of the ring but was more pronounced. Thick intrusions (Fig. 12d) propagated at alloy grain boundaries, encircling some alloy grains. Globular precipitates (Fig. 12e) were formed mainly at alloy grain boundaries ahead of the intrusions.

The scale outer region (Fig. 12b) was rich in Fe and Cr and contained small amounts of Ni. It probably consisted of Fe-oxides and $(FeNi)Cr_2O_4$. The inner region (Fig. 12c) was richer in Cr, less rich in Fe and Ni, and contained small amounts of S; this region was composed of $Cr_2O_3$ and a small amount of CrS. The intrusions (Fig. 12d) were primarily composed of $Cr_2O_3$ and variable amounts of Cr-Mn-S solid solution. Analysis of the globular precipitates confirmed that they consisted of a Cr-Mn-S solid solution.

310 - Particular Features

Coarse, widely-spaced precipitates were found in Type 310 stainless steel (Fig. 13A-D). These precipitates were present in the full cross-section of the alloy (Fig. 13B) but were absent in a Cr-denuded region about 50 μm deep adjacent to the scale (Fig. 13A). AES analysis confirmed that these precipitates were sigma phase. The chromium content of the sigma phase and the surrounding matrix were 39.5 and 18 wt %, respectively. The AE map (Fig. 13d) for the area shown in Fig. 13c demonstrates this variation in the chromium content. The volume fraction of the sigma phase increased with time (2).

HK40

A typical cross-section of an HK40 sample is shown in Fig. 14. An electron image and the corresponding X-ray maps are included in Fig. 15.

No deposit was found on this sample. The scale (Fig. 14a,b) was irregular in thickness and, apparently, had spalled over large areas. Long intrusions (Fig. 14c), 300 μm deep, extended into the alloy along the interdendritic boundaries. Internal precipitation (Fig. 14d,e) occurred in the alloy, but to a small depth compared with the intrusions. The volume fraction and size of the precipitates decreased with depth.

At locations where the scale was relatively thick, an outer light-grey layer (Fig. 14a) and an inner darker-grey layer (Fig. 14b) were identified. These layers were of similar composition to the scale (Fig. 12b,c) formed on the bottom of the 347H ring except that some Mn was found in the HK40 sample. Intrusions along the interdendritic boundaries (Fig. 14c) were composed of $Cr_2O_3$ and CrS. Although the coarse (Fig. 14d) and fine (Fig. 14e) precipitates were primarily CrS, the presence of $Cr_2O_3$ in the precipitation zone cannot be definitely ruled out. The alloy within this zone was depleted in chromium.

253MA

A cross-section of a 253MA sample is shown in Fig. 16. An electron image and the corresponding X-ray maps of all the detected elements are included in Fig. 17. It was evident that the scale and the deposit had spalled at many locations leaving only an adherent subscale. The attack was localized in the form of large "pits" (Fig. 16a,b), intrusions (Fig. 16d) along twin and grain boundaries and intergranular penetrations (Fig. 16e) to a depth of ~200 μm. In addition, a different type of precipitate (Fig. 16f) extended to a much greater depth within the alloy grains.

Analysis of the corrosion products contained within the "pit" (Fig. 16a,b) was complicated because of entrapped alloy particles that were composed primarily of Fe and Ni. The main feature was the presence of an irregular Cr-rich film (Fig. 16c) at the bottom of the pit. This film was probably $Cr_2O_3$ containing a relatively large volume fraction of CrS. The intrusions (Fig. 16d) and the intergranular precipitates (Fig. 16e) were composed primarily of $Cr_2O_3$ and CrS; however, the precipitates contained a larger proportion of CrS. As is evident in the X-ray maps, enrichment in Si occurred principally in the regions adjacent to the film, intrusions and intergranular precipitates. Some association between the oxygen and silicon distribution was evident; therefore, most probably a thin $SiO_2$ film or discreet precipitates existed in these areas. This high concentration of Si is intriguing considering that this alloy contains only 1.5 wt % Si.

As alluded to earlier, precipitation within the alloy grains occurred to a much greater depth than in the S-rich intergranular precipitates. The morphology of these intragranular precipitates can be seen in Fig. 18A. In

this sample, the S-rich intergranular precipitates were ∿150 μm deep, whereas the platelet-like intragranular precipitates extended to a depth of ∿800 μm. The latter were less than 1 μm thick and their length was quite variable. Within each grain, the precipitates grew in well-defined directions which varied from one grain to another. The volume fraction of these oriented precipitates decreased with depth and their morphology became less defined, Fig. 18B. Precipitation at grain and twin boundaries also occurred to a greater depth ahead of the S-rich intergranular precipitates. A precipitate-free zone was evident in the contiguous regions.

EPMA indicated that the oriented, intergranular and twin-boundary precipitates were rich in Cr. The Fe and Ni signals probably arose from the surrounding alloy matrix. The carbon level in the precipitates was only a few counts higher than the matrix. Sample contamination by carbon (from residual gases in the instrument and from metallographic preparation) vitiated determinations of the carbon content of precipitates by AES analysis.

Incoloy 800H

Scales formed on Incoloy 800H and 253MA were similar; although the former alloy was generally internally attacked to a greater depth (2).

As illustrated in Fig. 19, the scale (Fig. 19a,b) exhibited localized intrusions (Fig. 19c) at alloy grain and twin boundaries. Intergranular attack (Fig. 19d) occurred to a depth of ∿600 μm. Intragranular precipitates (Fig. 19e) were non-uniformly distributed and occurred to a depth usually less than that of the intergranular attack.

The outer region of the scale (Fig. 19a) was $Cr_2O_3$ containing small amounts of S, Fe and Ni. The inner region (Fig. 19b) contained a large volume fraction of CrS. The thick intrusions (Fig. 19c) and the intergranular precipitates (Fig. 19d) were composed of $Cr_2O_3$ and CrS similar to the observations made on 253MA alloy. The intragranular precipitates (Fig. 19e) were primarily composed of CrS.

Similar, also to the observations on the 253MA alloy, Cr-rich, oriented transgranular precipitates, as well as intergranular and twin-boundary precipitates were found. The transgranular precipitates extended to a depth much greater than the S-rich precipitates; whereas the intergranular and twin-boundary precipitates extended across the full section of the ring. Twin-boundary precipitates are better revealed by deep-etching, Fig. 20.

As shown in Fig. 21, at some locations beneath the scale, an irregularly-shaped phase (Fig. 21a) appeared in the form of large patches. This phase was associated with the alloy grain boundaries and was composed primarily of Cr and S, together with small amounts of Mn as well as a highly variable amount of oxygen. It also contained some Si, although the concentration of this element was not determined. A region containing this phase is shown at higher magnification in Fig. 22. The X-ray maps confirmed that this phase was composed of Cr, Mn, Si and S. The alloy grain boundaries contained a higher concentration of Si, which appeared to be associated with a discontinuous $SiO_2$ film. The matrix surrounding the patch-like phase was rich in Fe and Ni but was depleted in Cr. Precipitates of various sizes were found in the vicinity: the smaller globular precipitates were composed of Cr, Mn and S, whereas the large precipitates were also rich in Si, similar to the patch-like phase.

The morphology of the patch-like phase and its spread over a large area suggested that it might have been molten at the temperature of exposure, 850°C. However, the alloy grain boundaries appeared to extend through this phase without being affected (Fig. 21 and 22). This would not be the case had the phase been molten. Examination of samples exposed for a longer period may resolve this issue.

Several uncooled Incoloy 800H samples suffered catastrophic attack with perforation occurring at the bottom of the ring (2). A cross-section in the vicinity of a perforation is shown in Fig. 23. An electron image and the corresponding X-ray maps are presented in Fig. 24.

The scale exhibited three distinct thick layers. The outer, dark-grey layer (Fig. 23a) was porous and was probably $Cr_2O_3$ containing small amounts of S, Fe, Ni, Si and Ti. The intermediate light-grey layer (23,b) was composed of Fe, Ni and large amounts of S. Large cavities and particles (Fig. 23d) - some possibly having a dendritic structure - were present in this layer. These particles were primarily composed of Fe and Ni. Probably, the (FeNi)S layer was molten at temperature and was saturated with both Fe and Ni, which precipitated upon cooling. The molten layer flowed and penetrated the outer layer at some locations (23,b). The inner-grey layer (Fig. 23c) was primarily composed of Fe, Cr, Ni and S. Cavities were present in this layer in the region adjacent to the alloy. Most of the internal

attack occurred intergranularly. The intergranular precipitates (Fig. 23e) were composed predominantly of $Cr_2O_3$ and some CrS; whereas the intragranular precipitates (Fig. 23f) contained a higher proportion of CrS.

## SUMMARY

The morphology of the attack on several commercial ferritic and austenitic Fe-based alloys exposed for up to 3 000 h in an AFBC charged with a sulphur-containing coal and a limestone sorbent has been described. The following conclusions can be made.

Behaviour of the ferritic alloys

The ferritic alloys (A1, T11, T22 and T91) form thick, adherent $Fe_3O_4$ scales containing dissolved Cr in proportion to the alloy chromium content (3 wt % for T22 and 14 wt % for T91).

The scales on T11, T22 and T91 are quite non-uniform microscopically and exhibit an undulating interface with the alloy. In T91, it was found that this morphology was associated with the development of a chromium-rich film (most likely $Cr_2O_3$). However, this film is not fully protective, as it is penetrated by sulphur.

Bed material (essentially $CaSO_4$, CaO, $SiO_2$ and $Al_2O_3$) deposits on the scales giving rise to highly heterogeneous outer layers which are rich in Fe-oxide in addition to the bed constituents. This outer layer is thicker at the top and is usually absent at the bottom, probably because of the highly erosive conditions prevailing in many regions of the bed.

The deposits of the T91 are the thickest and most adherent and seem to protect the alloy from the erosive action of the fluidized bed.

Because of the fine grain size and extreme heterogeneity of the outer layer, it was not possible to establish conclusively whether chemical interaction occurs between the iron-rich scales and the deposit.

The sulfidation attack on these alloys is quite limited and occurs in the form of an FeS grain boundary network in the inner region of the $Fe_3O_4$ scale on carbon steel or in the form of internal $Cr_xS_y$ precipitates in the other alloys.

Behaviour of the austenitic alloys

The attack on the austenitic alloys can be extremely non-uniform and consists of a thin scale and an internal precipitation zone.

The scales spalled readily and were heavily damaged. Typically, they are composed of a relatively thick heterogeneous outer layer rich in Fe, Ni, Cr and Mn (probably in the form of $MCr_2O_4$ where M = Fe, Ni or Mn, and remnant transient NiO and $Fe_2O_3$) and an inner thin $Cr_2O_3$ film. It is only at a later stage that a varying amount of sulphur, in the form of $Cr_xS_y$, is detected in the inner region.

Internal attack, the predominant degradation mechanism, is influenced by alloy microstructure. For example, it propagates preferentially along the interdendritic phase in HK40 and along grain boundaries in the other alloys, forming thick localized intrusions composed of predominantly $Cr_2O_3$ and small amounts of $Cr_xS_y$. The amount of $Cr_xS_y$ increases with depth. The precipitates formed in the dendrites in HK40 and those formed within the grains in the other alloys are probably $Cr_xS_y$.

Types 304H, and 310 stainless steels are more resistant to this type of degradation than the other austenitic alloys. The grain size of these alloys is relatively small (ASTM GS:5). Enhanced oxygen/sulphur diffusion along the boundaries of the coarse grains of Incoloy 800H (ASTM GS:0-00) and along the interdendritic phase in HK40 was probably responsible for the poor performance of these alloys. In addition, these two alloys as well as 253MA contain a $Cr_xS_y$ network which would enhance the nucleation and growth of $Cr_2O_3/Cr_xS_y$.

Incoloy 800H, exposed in this environment at 850°C, is susceptible to catastrophic failure induced by the formation of molten Ni-Fe-S.

## ACKNOWLEDGEMENTS

The authors express their appreciation to C.W. Cuzner, Y. Lafreniére and R. Poirier for the metallographic preparation. They are grateful to Mrs. V.E. Moore for the electron-probe microanalyses, to Messrs E. Cousineau and E. Murray for the XRD analyses and to Mr. K. Gaugler of Lawrence Berkeley Laboratory for the Auger electron spectroscopic observations. The authors are indebted to Drs. R.W. Revie and D.W.G. White for reviewing the report.

## REFERENCES

1. Gilmour, J.B. Lui, A.W., Briggs, D.C. and Hindam, H. "The EMR/NSPC AFBC Materials Programme: Alloys and Procedures"; Division Report ERP/PMRL 85-11; February 1985.

2. Gilmour, J.B., Hindam, H., Lui, A.W. and Briggs, D.C. "The EMR/NSPC AFBC Materials Programme: Evaluation of Probes"; Division Reports; 1985.

3. Gilmour, J.B., Briggs, D.C., Lui, A.W. and Hindam, H. "Preliminary results of the Canadian AFBC materials tests"; Corrosion/85, Paper No. 341, National Association of Corrosion Engineers, Boston, Massachussetts, 1985.

4. Gilmour, J.B., Hindam, H. Lui, A.W., Briggs, D.C. and Knight, R.F. "Selected results after 500-h exposure in the Canadian AFBC program"; Corrosion/86, Paper No. 91, National Association of Corrosion Engineers, Houston, Texas (1986).

Table 1 - Experimental conditions

| Sample | Alloy | T(C) | | t(h) |
|---|---|---|---|---|
| | | Top | Bottom | |
| 2A1-1 | A1 | 539 | 392 | 1000 |
| 2A1-8 | A1 | 613 | 515 | 1000 |
| 2A1-7 | T11 | 602 | 497 | 1000 |
| 2A1-3 | T22 | 560 | 427 | 1000 |
| 2A1-10 | T22 | 627 | 535 | 1000 |
| 2A1-14 | T22 | 638 | 562 | 1000 |
| 2A1-18 | T22 | 634 | 577 | 1000 |
| 2A2-14 | T22 | 561 | 517 | 3000 |
| 2A1-11 | T91 | 633 | 545 | 1000 |
| 2A2-11 | T91 | 554 | 504 | 3000 |
| 2A2-19 | T91 | 570 | 540 | 3000 |
| 2A1-12 | 304H | 640 | 555 | 1000 |
| 2A2-16 | 304H | 565 | 526 | 3000 |
| 3B1-3 | 304H | 637 | 615 | 2000 |
| 10DL1-7 | 347H | 850 | | 1000 |
| 10DL2-7 | 347H | 850 | | 3000 |
| 10DL2-8 | 310 | 850 | | 3000 |
| 10DL2-13 | 310 | 850 | | 3000 |
| 10DL2-18 | 310 | 850 | | 3000 |
| 10DL1-19 | HK40 | 850 | | 1000 |
| 10DL2-19 | HK40 | 850 | | 3000 |
| 10DL1-5 | 253MA | 850 | | 1000 |
| 10DL2-15 | 253MA | 850 | | 3000 |
| 9DL2-20 | 253MA | 850 | | 3000 |
| 1B1-16 | 800H | 850 | | 5000 |
| 10DL1-6 | 800H | 850 | | 1000 |
| 10DL2-6 | 800H | 850 | | 3000 |
| 9DL2-6 | 800H | 850 | | 3000 |

Table 2 - Chemical composition (wt %) of alloys

| Alloy | C | Mn | S | P | Si | Cr | Ni | Mo | Nb | N | Al | Cu | Other |
|---|---|---|---|---|---|---|---|---|---|---|---|---|---|
| A1 (CS) | .19 | .60 | .022 | .010 | .16 | | | | | | | | |
| T11 | .12 | .52 | .010 | .013 | .73 | 1.30 | | .5 | | | | | |
| T22 | .13 | .49 | .022 | .025 | .28 | 2.12 | | .88 | | | | | |
| T91 | .10 | .38 | .005 | .014 | .40 | 8.45 | .11 | .96 | .076 | .039 | .005 | .02 | 0.23 V |
| 304H | .04 | 1.22 | .005 | .015 | .54 | 18.24 | 9.77 | | | | | | |
| 310 | .079 | 1.60 | .018 | .021 | .46 | 24.17 | 19.93 | | | | | | |
| 347H | .058 | 1.64 | .005 | .036 | .48 | 17.26 | 10.11 | | .75 | | | | .01 Ta |
| 800H | .074 | .96 | .001 | | .55 | 20.58 | 33.34 | | | | .33 | .20 | .35 Ti |
| HK40 | .40 | .86 | .014 | .022 | 1.40 | 24.91 | 20.20 | .099 | | | | | |
| 253MA | .08 | .42 | .003 | .016 | 1.53 | 20.82 | 10.89 | | | .018 | | | .03 Ce |

Table 3 - X-ray diffraction results

| Sample | Composition | Phases detected |
|---|---|---|
| 2A1-1 | A1 | $Fe_3O_4$*, $Fe_2O_3$, $CaSO_4$ |
| 2A1-8 | A1 | $Fe_3O_4$*, $CaSO_4$ |
| 2A1-7 | T11 | $Fe_3O_4$ |
| 2A1-3 | T22 | $Fe_3O_4$*, $Fe_2O_3$, $CaSO_4$ |
| 2A1-10 | T22 | $Fe_3O_4$*, $Fe_2O_3$, $CaSO_4$ |
| 2A1-18 | T22 | $Fe_3O_4$*, $Fe_2O_3$, $CaSO_4$ |
| 2A1-11 | T91 | $Fe_3O_4$*, $Fe_2O_3$, $CaSO_4$ |
| 2A1-12 | 304H | $Fe_3O_4$*, $Fe_2O_3$, $CaSO_4$ |
| 2A2-16 | 304H | $Fe\ Cr_2O_4$ |
| 10DL1-19 | HK40 | $(FeCr)_3O_4$, $Fe_3O_4$, $Fe_2O_3$, $CaSO_4$ |
| 10DL1-5 | 253MA | $Cr_2S_3$, $Cr_2O_3$, $FeCr_2O_4$, $Fe_3O_4$, $Fe_2O_3$, $CaSO_4$ |
| 1B1-16 | 800H | $Cr_2O_3$, $FeCr_2O_4$, $(FeCr)_3O_4$, $Fe_2O_3$, $CaSO_4$ |

*Major phase

Table 4 - Typical composition (wt %) of bed material

| | | | |
|---|---|---|---|
| CaO | 23.7 | $K_2O$ | 2.3 |
| $SiO_2$ | 37.2 | $Na_2O$ | 0.28 |
| $Al_2O_3$ | 15.6 | S | 4.1 |
| $Fe_2O_3$ | 2.7 | C | 0.54 |
| MgO | 1.8 | | |

Fig. 1 - Carbon steel (A1), top of the ring, exposed at 613°C for 1000 h.

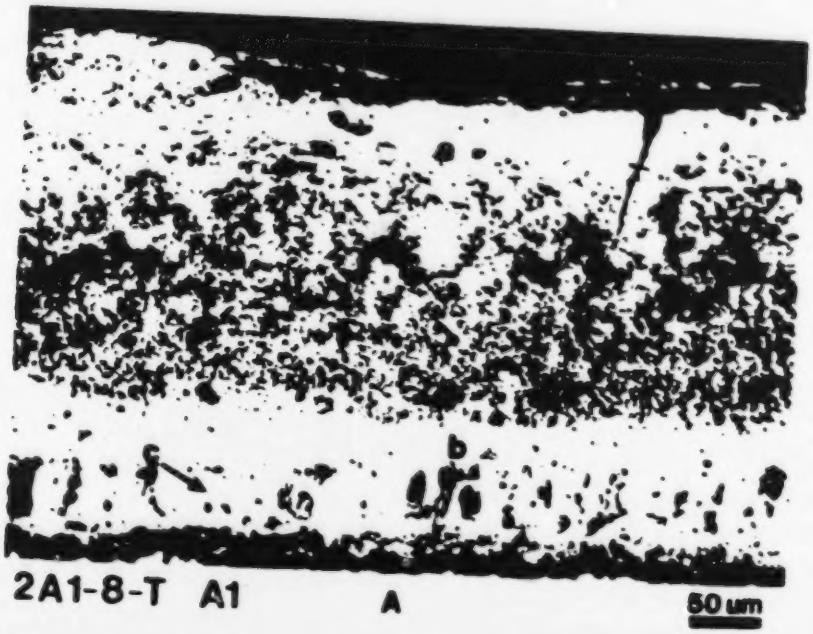


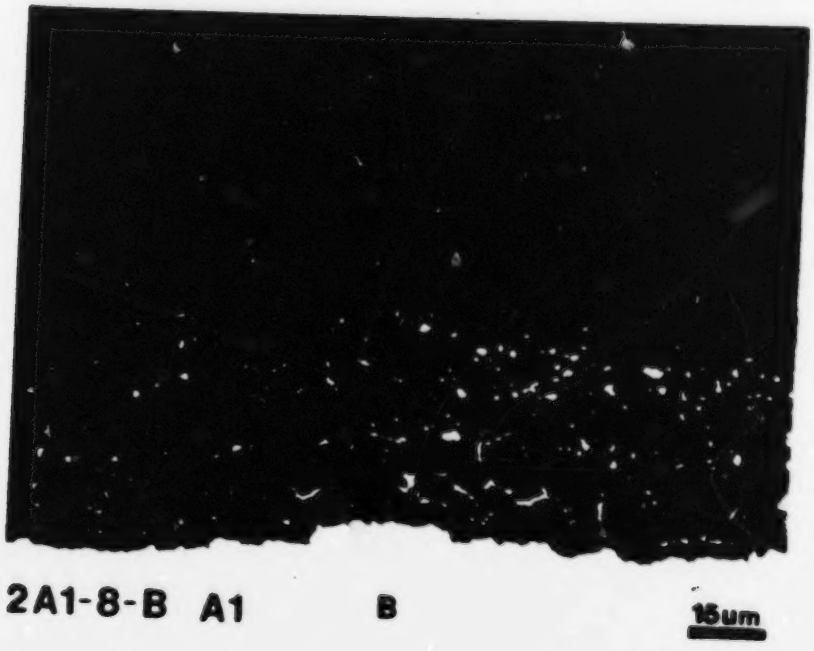

Fig. 2 - Type T22 alloy, top of the ring, exposed at 561°C for 3000 h.

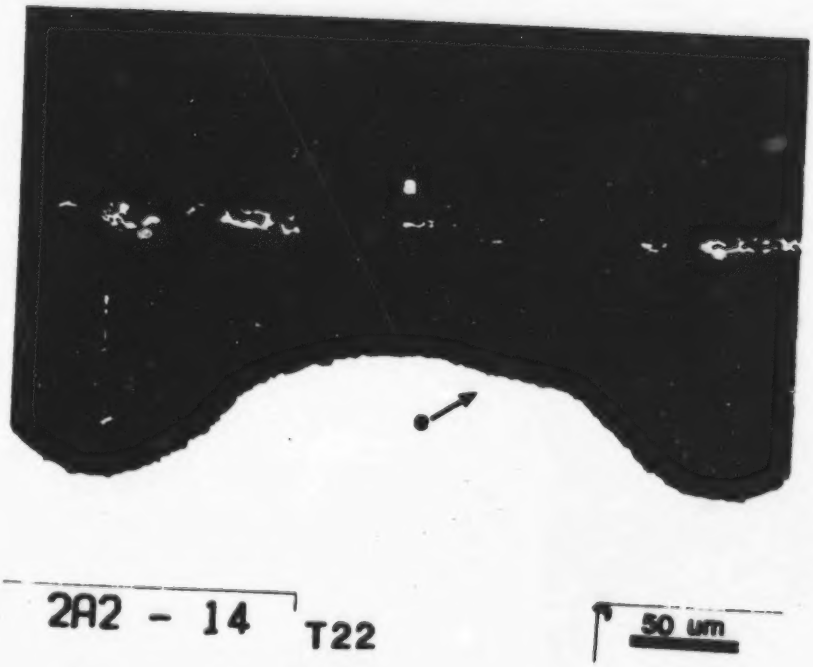


| Feature | Position | S | Ca | Cr | Mn | Fe | Ni | O |
|---|---|---|---|---|---|---|---|---|
| Deposit | 2,a | 1.5-4 | 7-26.5 | -- | -- | 29.4-57.5 | -- | 33.7-42.9 |
| | | (1.4-3.3) | (5.1-17.2) | | | (13.7-30.6) | | (62.7-69.8) |
| Scale | 2,b | 0.1-0.5 | 0.5-0.7 | 2.8-3.2 | -- | 61.4-65.6 | -- | 30.5-34.3 |
| | | (0.1-0.5) | (0.3-0.5) | (1.6-1.9) | | 33-37.2 | | (60.4-64.4) |
| Streaks | 2,c | 28.1 | -- | -- | -- | 60.6 | -- | 10 |
| | | (33.5) | | | | (41.5) | | (24) |
| Stringer | 2,d | 12.4-13.3 | -- | 1.9-2.2 | -- | 62.4-63.5 | -- | 21.6 |
| | | (13.2-14.1) | | (1.2-1.4) | | (38.1-38.9) | | (46) |
| Internal | 2,e | 0.5-0.9 | -- | 5.2 | -- | 81.8-83.5 | -- | 9.9-10.8 |
| Precipitates | | (0.7-1.3) | | (4.5) | | (63.9-66.6) | | (27.5-29.5) |

Fig. 3 - Electron image and X-ray maps of the sample shown in Fig. 2.

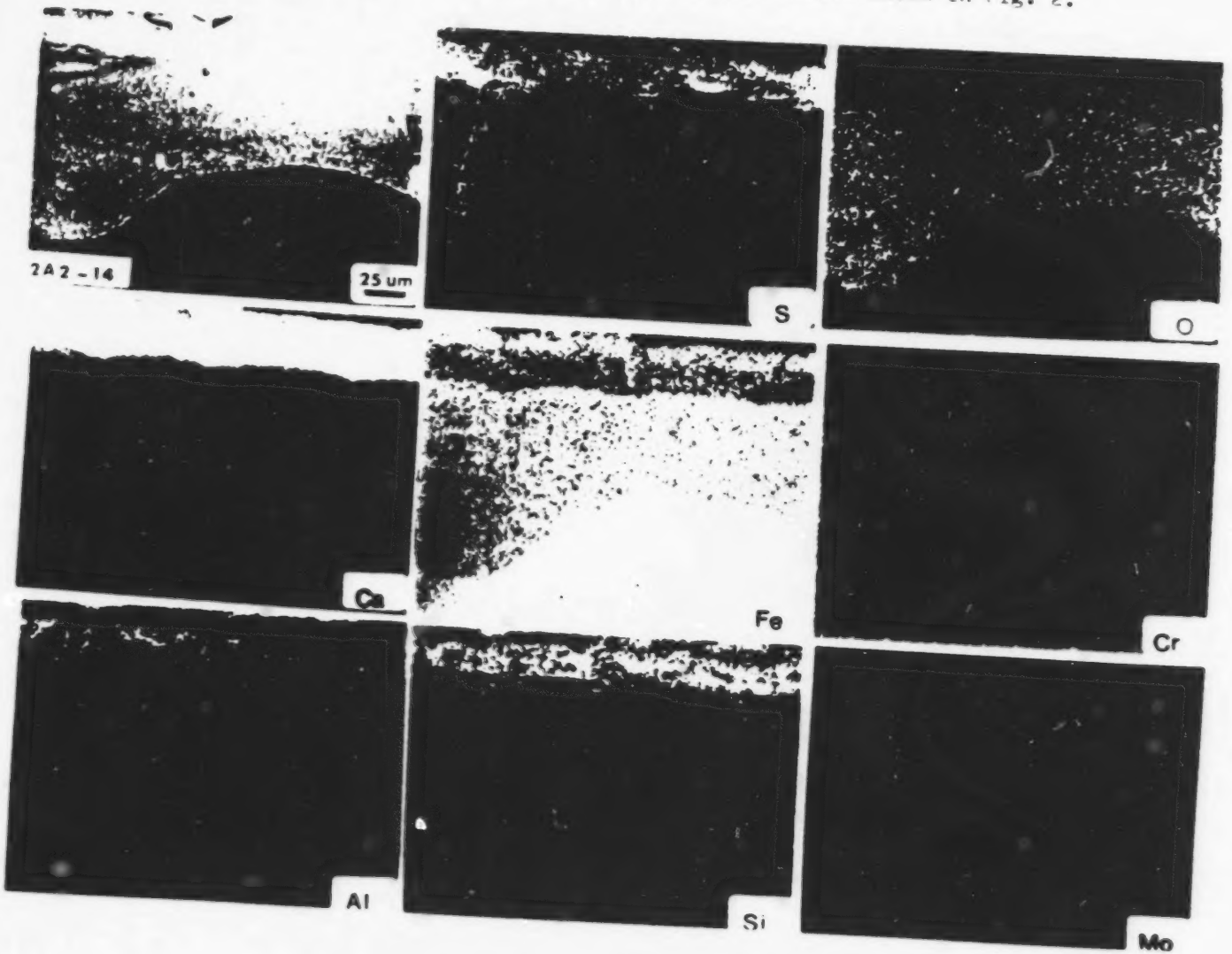

Fig. 4 - Type T91 alloy, top of the ring, exposed at 570°C for 3000 h.

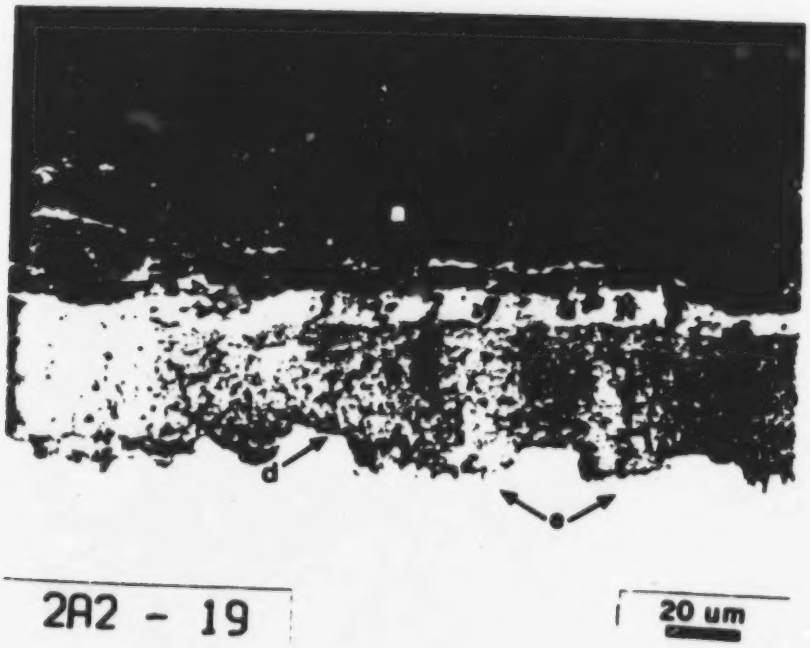


| Feature | Position | S | Ca | Cr | Mn | Fe | Ni | O |
|---|---|---|---|---|---|---|---|---|
| Deposit | 4,a | 3.4-11.2 | 6-22.8 | -- | -- | 26.8-40.9 | -- | 31.4-39.6 |
| | | (3.2-9.1) | (4.5-14.8) | | | (12.5-32.1) | | (59.9-66.4) |
| Scale | 4,b | -- | -- | 13-13.8 | -- | 51.8-54.3 | -- | 32.3-33.8 |
| | | | | (7.7-8.0) | | (27.9-29.9) | | (62.1-63.7) |
| Streaks | 4,c | 32.3-35.9 | -- | -- | -- | 60 | -- | 3.1-6.4 |
| | | (40.1-46.5) | | | | (44) | | (7.9-16) |
| Inner Film | 4,d | -- | -- | 20.6-27 | -- | 42.9-48.9 | -- | 29.4 |
| | | | | (12.6-16.5) | | (24.5-28) | | (58.6) |
| Internal Precipitates | 4,e | -- | -- | 13.1-15.2 | -- | 68.5-69.7 | -- | 14.4-17.2 |
| | | | | (9.8-11.9) | | (47.6-50.8) | | (36.8-41.7) |

Fig. 5 - Photo-micrograph of a deeply-etched T91 sample showing inner film (arrow); sample exposed at 633°C for 3000 h.

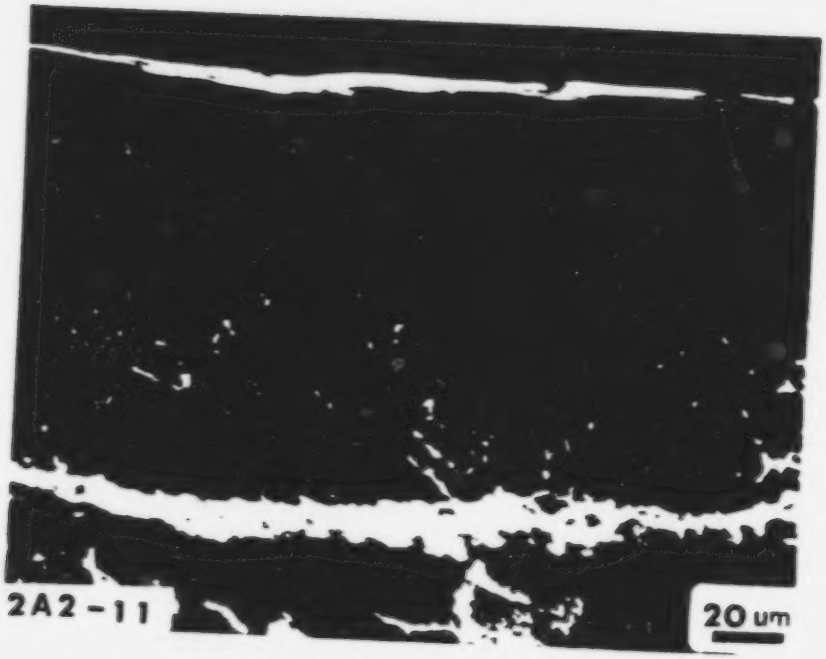

Fig. 6 - Bottom of the ring whose top is shown in Fig. 4. (T = 540°C).

| Feature | Position | S | Ca | Cr | Mn | Fe | Ni | O |
|---|---|---|---|---|---|---|---|---|
| Scale | 6,a | 0.3 | -- | 10.6 | -- | 58.2 | -- | 30.3 |
| | | (0.3) | | (6.4) | | (32.9) | | (59.9) |
| Streaks | 6,b | 16.1-20.4 | -- | 10.2-11.5 | -- | 53.8-54.4 | -- | 14.8-18.3 |
| | | (17.7-23.2) | | (7.2-7.8) | | (34-35.6) | | (33.7-40.3) |
| Internal | 6,c | 0.8-2.3 | -- | 18.6-25.8 | -- | 46.4-61 | -- | 17.4-26.4 |
| Precipitates | | (0.9-2.7) | | (13.7-17.3) | | (27.6-41.7) | | (41.4-54.7) |

Fig. 7 - Electron image and corresponding X-ray maps of a T91 sample which was exposed at 633°C for 1000 h.

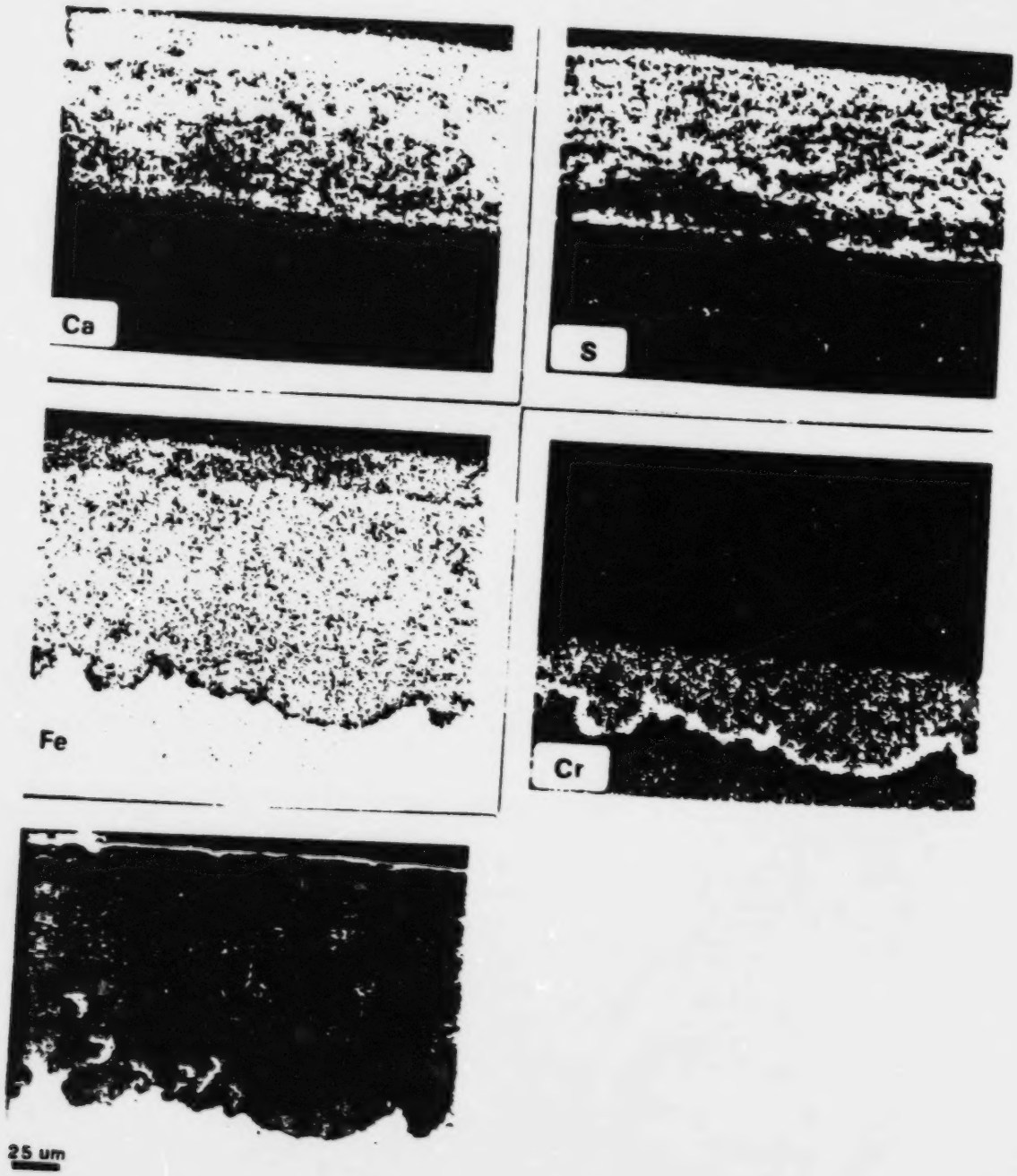

Fig. 8 - Type 310 stainless steel, bottom of the ring, exposed at 850°C for 3000 h.

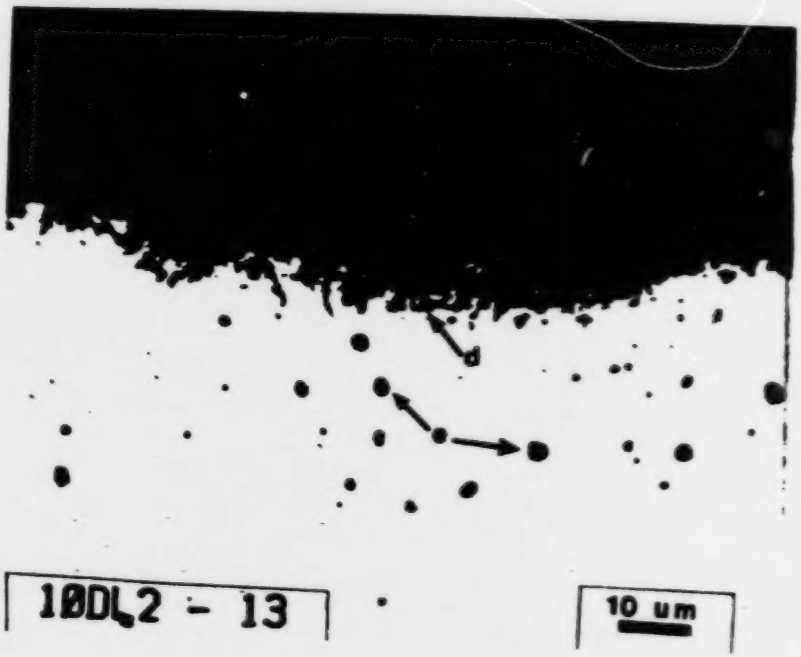


| Feature | Position | S | Cr | Mn | Fe | Ni | O |
|---|---|---|---|---|---|---|---|
| Scale | 8,a | -- | 49.3-54 | 0.4-0.7 | 8.1-10.2 | 0.9 | 36.7-38.8 |
| outer region | | | (26.4-29.7) | (0.2-0.4) | (4.1-5.1) | (0.4) | (61-65.5) |
| Scale | 8,b | -- | 14.2-15 | 0.6-2.3 | 36.6-49.3 | 4.3-15.3 | 30.9-31.2 |
| inner region | | | (8.6-9.1) | (0.4-1.3) | (20.6-27.6) | (2.3-8.2) | (60.8-61.0) |
| Inner film | 8,c | -- | 56.2 | -- | 8.9 | -- | 33.7 |
| | | | (32.1) | | (4.7) | | (62.6) |
| Intrusions | 8,d | -- | 40.8 | -- | 27.4 | 11.7 | 19.8 |
| | | | (28.9) | | (18.1) | (7.3) | (45.5) |
| Globular | 8,e | 25-30.4 | 8.8-18.2 | 32.6-44.7 | 8.4-19.1 | 2.7-6.5 | 3.2-5.5 |
| Precipitates | | (33.9-40.2) | (7.2-14.2) | (25.9-34.4) | (6.1-14.9) | (1.9-4.8) | (8.6-14) |

Fig. 9 - Electron image and corresponding X-ray maps for the sample shown in Fig. 8.

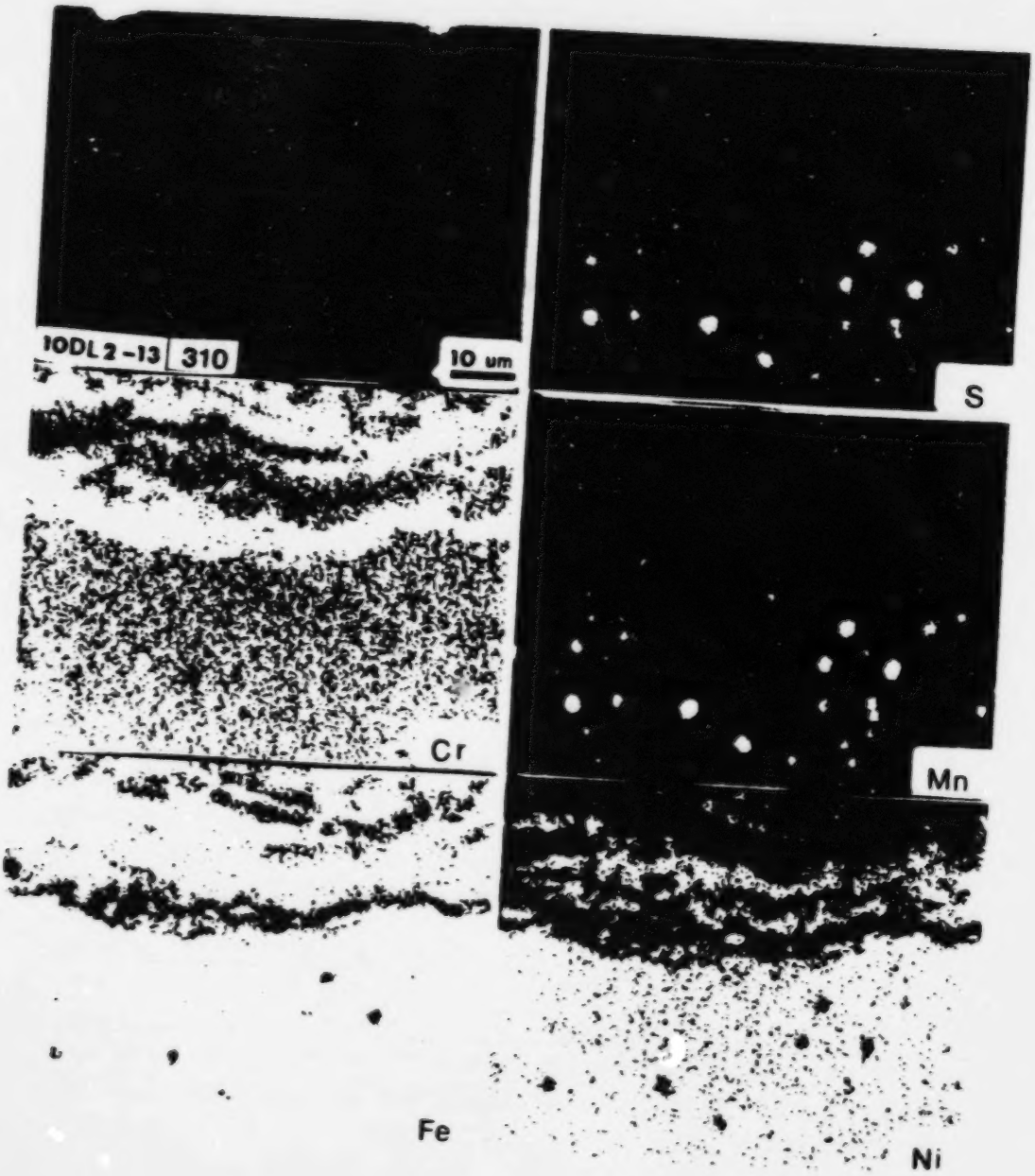

Fig. 10 - Auger electron spectrum of the globular precipitates formed in type 310 stainless steel; sample exposed at 850°C for 3000 h.

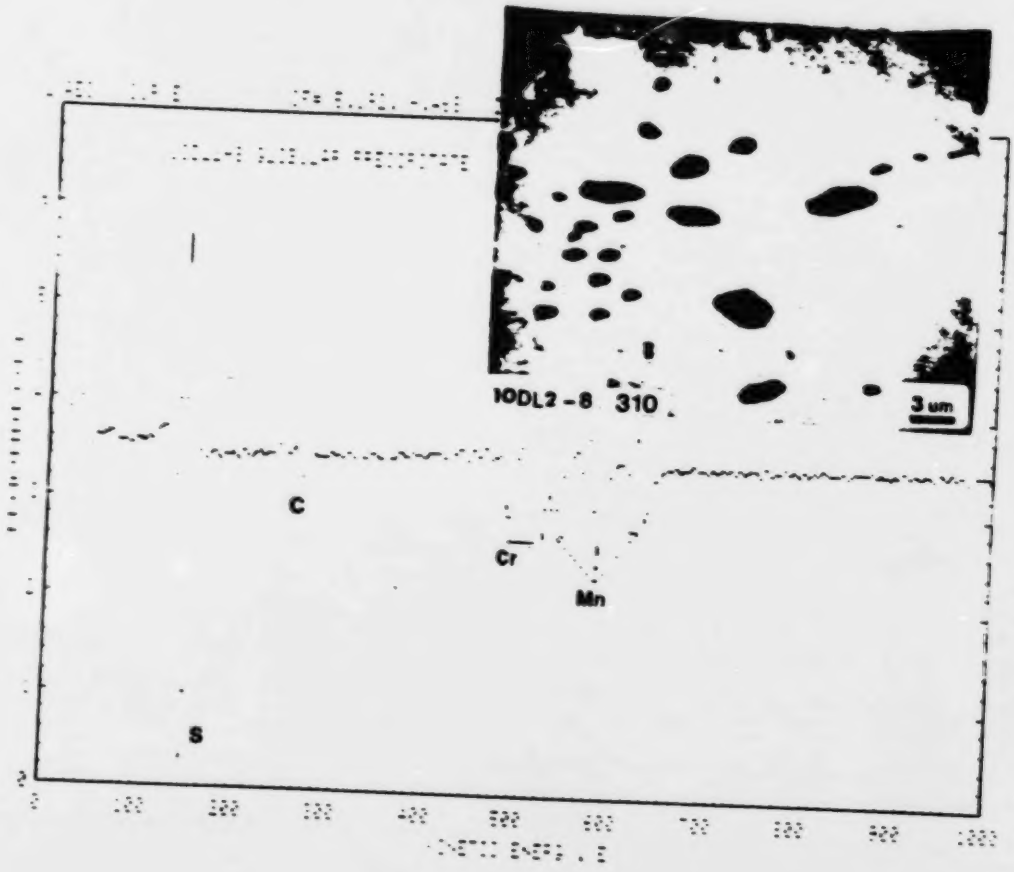

Fig. 11 - Type 347H stainless steel, top of the ring, exposed at 850°C for 3000 h.

10DL2 - 7

20 um

| Feature | Position | S | Ca | Cr | Mn | Fe | Ni | O |
|---|---|---|---|---|---|---|---|---|
| Deposit | 11,a | 0.2-3.1 (0.1-2.1) | 20.1-24.3 (10-13) | -- | 0.2-1.1 (0.1-0.4) | 6.6-16.8 (2.3-6.6) | -- | 57.7-72.3 (79.3-87.5) |
| Scale outer region | 11,b | -- | -- | 46.8-47.7 (23.6-26.2) | 3.1-7.7 (1.5-4) | 5.6-7.1 (2.6-3.6) | -- | 36.7-43.8 (65.5-71.8) |
| Scale inner region | 11,c | 2.7 (2.6) | -- | 61.7 (35.8) | 2.1 (1.2) | 1.6 (0.9) | -- | 31.4 (59.2) |
| Internal Precipitates | 11,d | -- | -- | 9.7-11 (4.4-6.6) | -- | 32.3-50.8 (13.7-28.7) | 3.7-6.5 (1.5-3.5) | 31 (61) |

Fig. 12 - Bottom of the ring whose top is shown in Fig. 11.

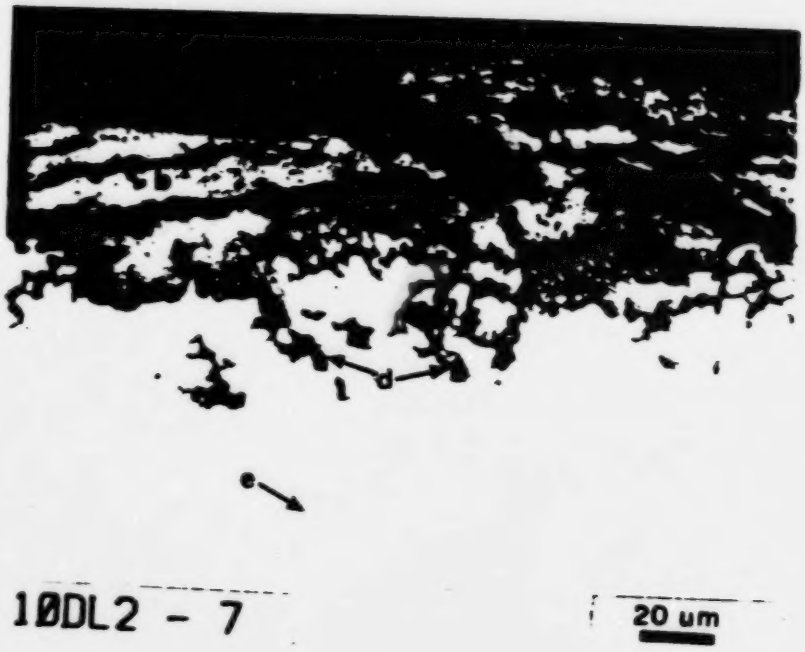


| Feature | Position | S | Ca | Cr | Mn | Fe | Ni | O |
|---|---|---|---|---|---|---|---|---|
| Deposit | 12,a | 1.8 (1.4) | 6.5 (4) | -- | -- | 42.4 (19) | -- | 48.1 (75) |
| Scale outer region | 12,b | -- | -- | 8.1-37.4 (4.6-21.1) | -- | 25.6-55.8 (13.4-29.5) | 0.2-2.9 (0.1-1.4) | 35.3-35.6 (64.6-66.3) |
| Scale inner region | 12,c | 2.2 (2.1) | -- | 59.1 (34.7) | -- | 6 (3.3) | 1.5 (0.8) | 30.9 (59) |
| Intrusions | 12,d | 1.4-10.8 (7.4-10) | -- | 44.6-48.1 (23.8-27.5) | 6.6-10.3 (3.3-5.6) | 2.5-3.2 (1.3-1.7) | -- | 30.6-36.8 (56.9-63.8) |
| Globular Precipitates | 12,e | 34.7-36.1 (46.4-48.3) | -- | 3.6-8.7 (3-7.1) | 51.1-56.5 (39.6-44.6) | 2.5-3.9 (1.9-3) | -- | -- |

Fig. 13 - Etched cross-sections depicting the sigma phase formed in type 310 stainless steel (a and b); electron image (c) and corresponding AE map of Cr (d).

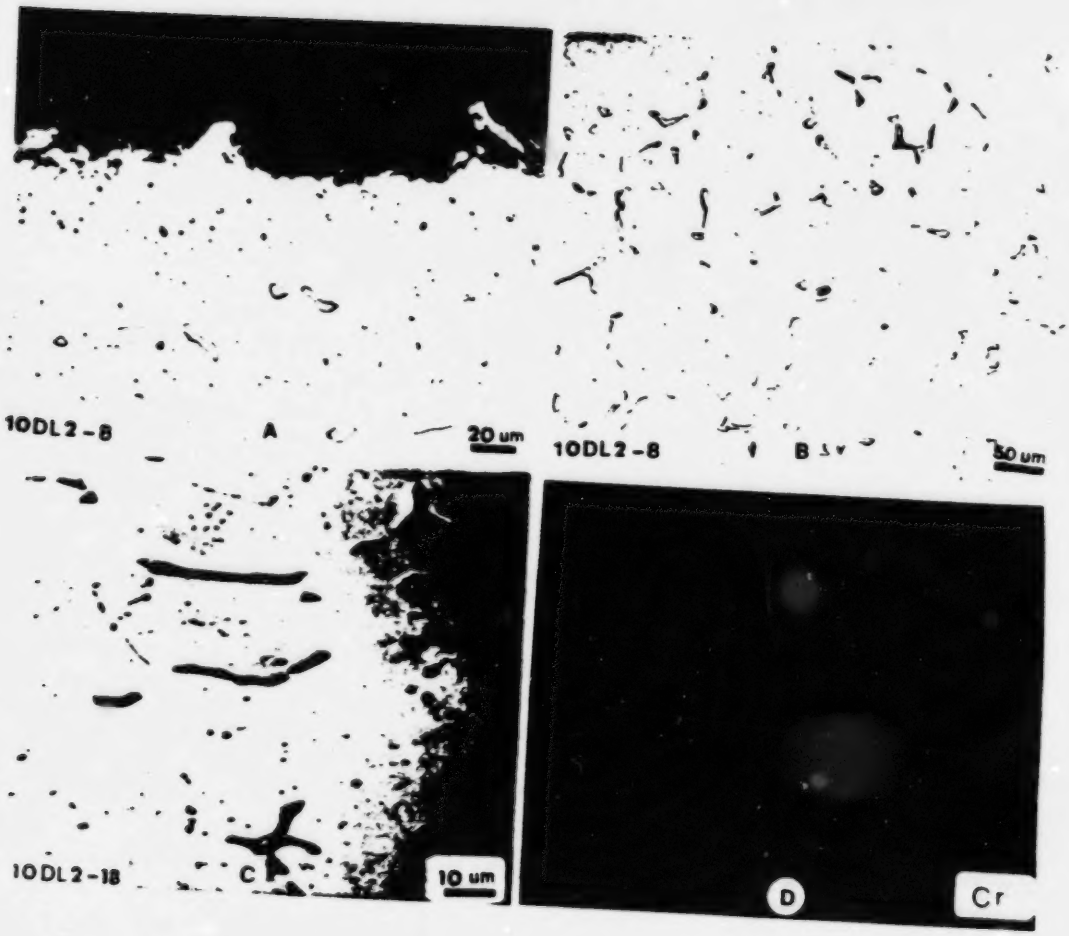

Fig. 14 - Type HK40 alloy, bottom of ring, exposed at 850°C for 3000 h.

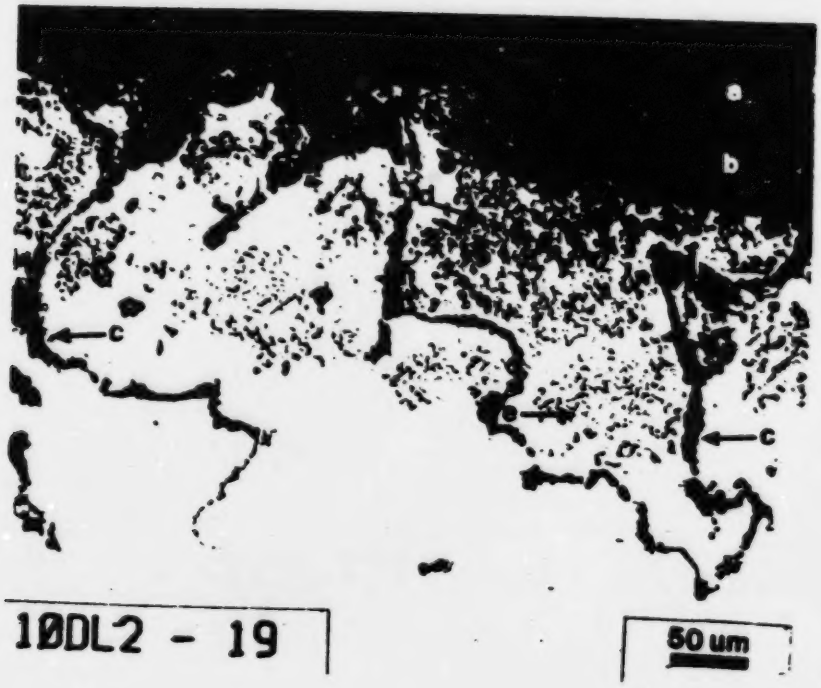


| Feature | Position | S | Ca | Cr | Mn | Fe | Ni | O |
|---|---|---|---|---|---|---|---|---|
| Scale | 14,a | -- | -- | 9.8-11.9 | 1-2.8 | 32.8-55.9 | 1.8-14.8 | 31.5-37.6 |
| outer region | | | | (5.9-6.6) | (0.5-1.5) | (16.9-31.2) | (1-7.3) | (61.4-67.7) |
| Scale | 14,b | 0.3-2.3 | -- | 60.5 | 0.4-1.1 | 0.9-3.6 | 0.8-1.7 | 33.7-35.1 |
| inner region | | (0.3-2.0) | | (33.9) | (0.2-0.6) | (0.5-1.9) | (0.4-0.9) | (62.3-63.3) |
| Intrusions | 14,c | 2.7-6.7 | -- | 20.6-51.3 | 0.7-1.2 | 3.8-11.9 | 2.3-8.5 | 36.4-55 |
| | | 2-5.6 | | (9.2-27.9) | (0.3-0.5) | (1.9-4.9) | (1.0-3.4) | (64.4-80) |
| Coarse | 14,d | 32.1-37.8 | -- | 53.4-54 | 1.5-2.0 | 0.8-2.0 | 0.7-1.8 | 2.5-11.5 |
| Precipitates | | (35.8-47.6) | | (36.7-42) | (1.0-1.5) | (0.5-1.4) | (0.5-1.2) | (6.3-25.6) |
| Fine | 14,e | 1.8-15.7 | -- | 8-30.4 | 0.7-1.4 | 16.6-38.3 | 12.3-31.0 | 19.5-30.4 |
| Precipitates | | (2.1-15.8) | | (5.8-18.8) | (0.4-0.9) | (9.6-25.7) | (6.8-19.8) | (45.7-58) |

Figure 15 - Electron image and corresponding X-ray maps for the sample shown in Fig. 14.

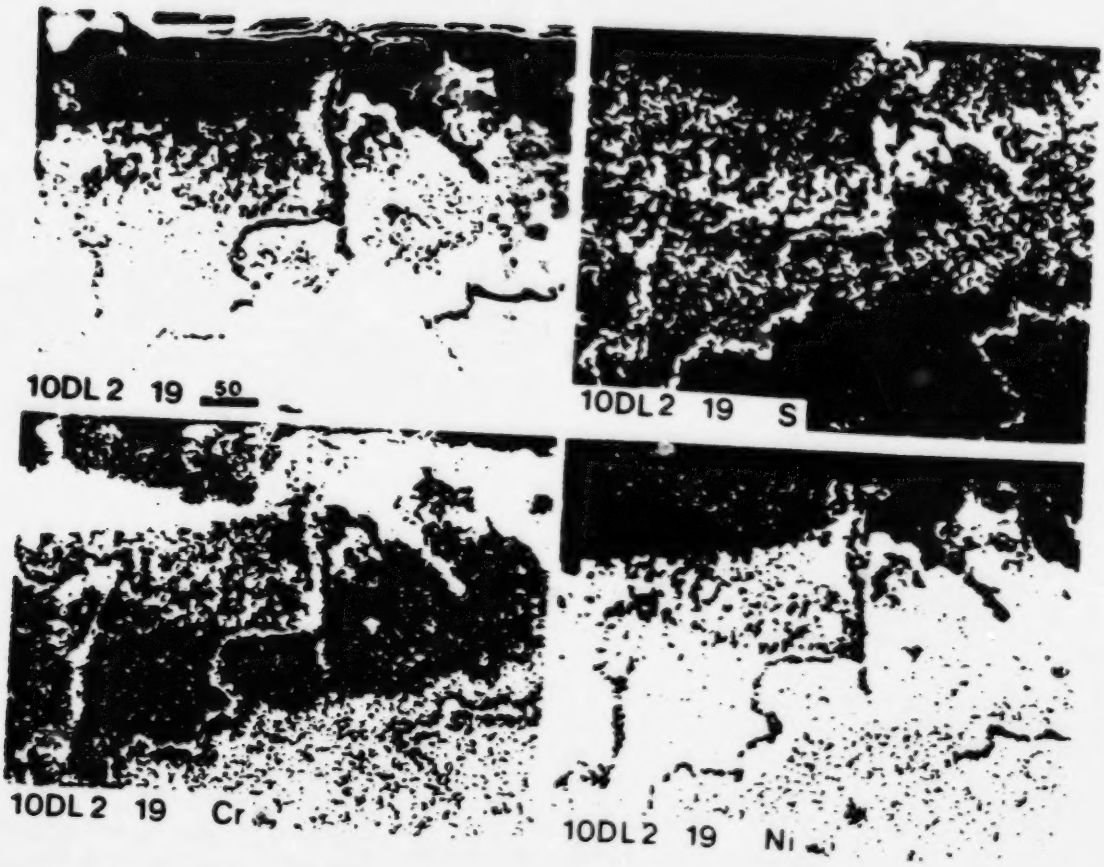

Fig. 16 - Type 253MA alloy, bottom of the ring, exposed at 850°C for 3000 h.

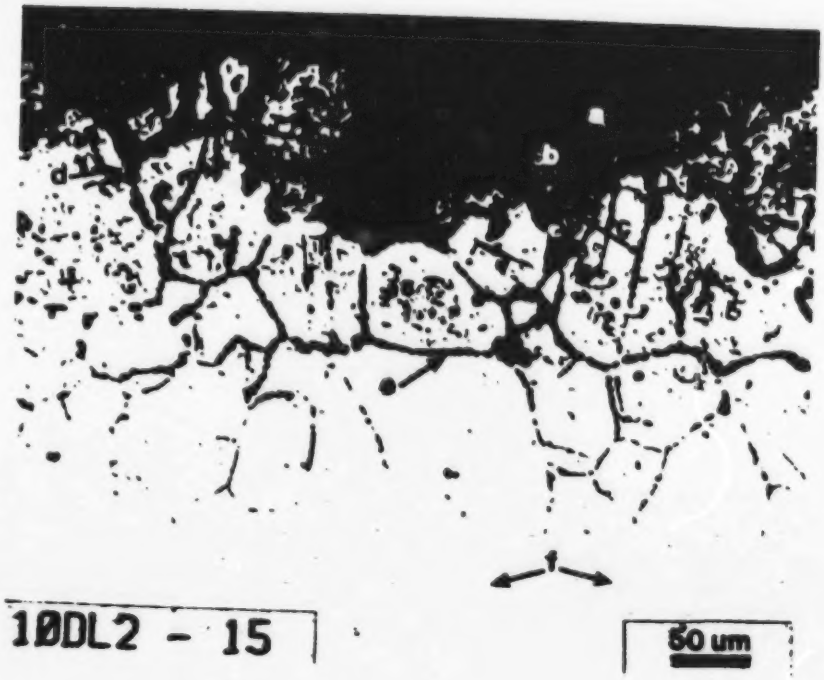


| Feature | Position | S | Ce | Cr | Mn | Fe | Ni | O |
|---|---|---|---|---|---|---|---|---|
| Pit | 16,a | 0.1-0.4 | -- | 25.3-39.9 | 1-1.3 | 26.4-41.4 | 0.6-1.6 | 30.7-31.3 |
| outer region | | (0.1-0.4) | | 15.1-23.9 | 0.6-0.8 | (14.7-23.0) | (0.3-0.9) | (59.7-60.8) |
| Pit | 16,b | 0.6-3.9 | -- | 4-13.3 | 1.7 | 37.4-46.6 | 1.7-26.6 | 26.6-36 |
| inner region | | (0.5-4.0) | | (2.5-7.5) | (1.0) | (22.2-24.4) | (0.8-15) | (65.3-65.8) |
| Inner | 16,c | 8.8 | -- | 58.8 | -- | 2.6 | 1.5 | 28.2 |
| Film | | (8.5) | | (34.9) | | (1.4) | (0.8) | (54.3) |
| Intrusion | 16,d | 0.6-3.7 | -- | 54.2-59.3 | -- | 2.9-7.2 | 1.4-5.1 | 30.5-35.3 |
| | | (0.6-3.4) | | (31.0-33.4) | | (1.5-4.0) | (0.7-2.7) | (58.8-64) |
| Intergranular | 16,e | 1.6-16 | -- | 43.2-58.2 | -- | 1.7-14.3 | 0.3-4.4 | 23.7-49.4 |
| Precipitates | | (1.4-16) | | (20.4-35.7) | | (1.0-7.6) | (0.2-2.2) | (62.2-75.7) |
| Intragranular | 16,f | -- | -- | 64.4-83 | -- | 4-21.2 | 0.3-2.7 | 11.5-14.6 |
| Precipitates | | | | (51.9-65) | | (2.9-15.9) | (0.2-1.9) | (30-36.1) |

Fig. 17 - Electron image and corresponding X-ray maps for the sample shown in Fig. 16.

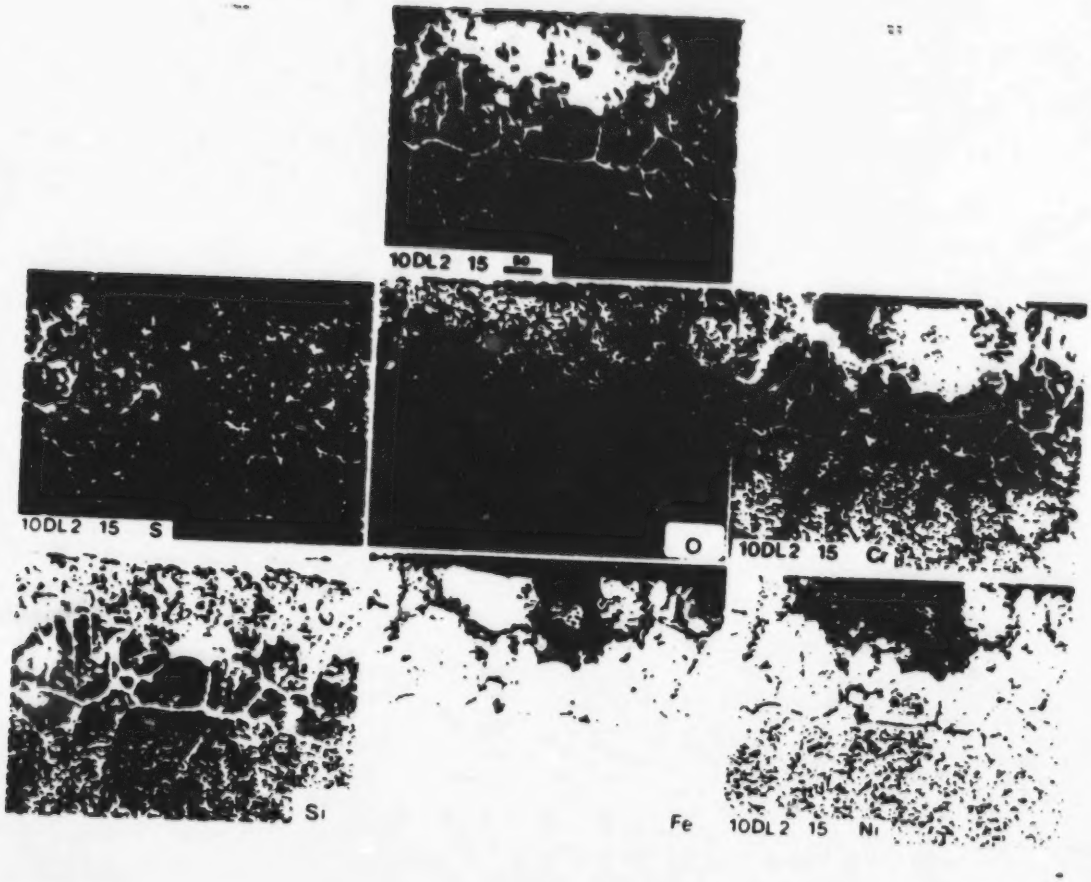

Fig. 18 - Etched cross-section of a 253MA sample showing the scale and the oriented platelet-like precipitates (a); morphology of these precipitates near the precipitation front (b).

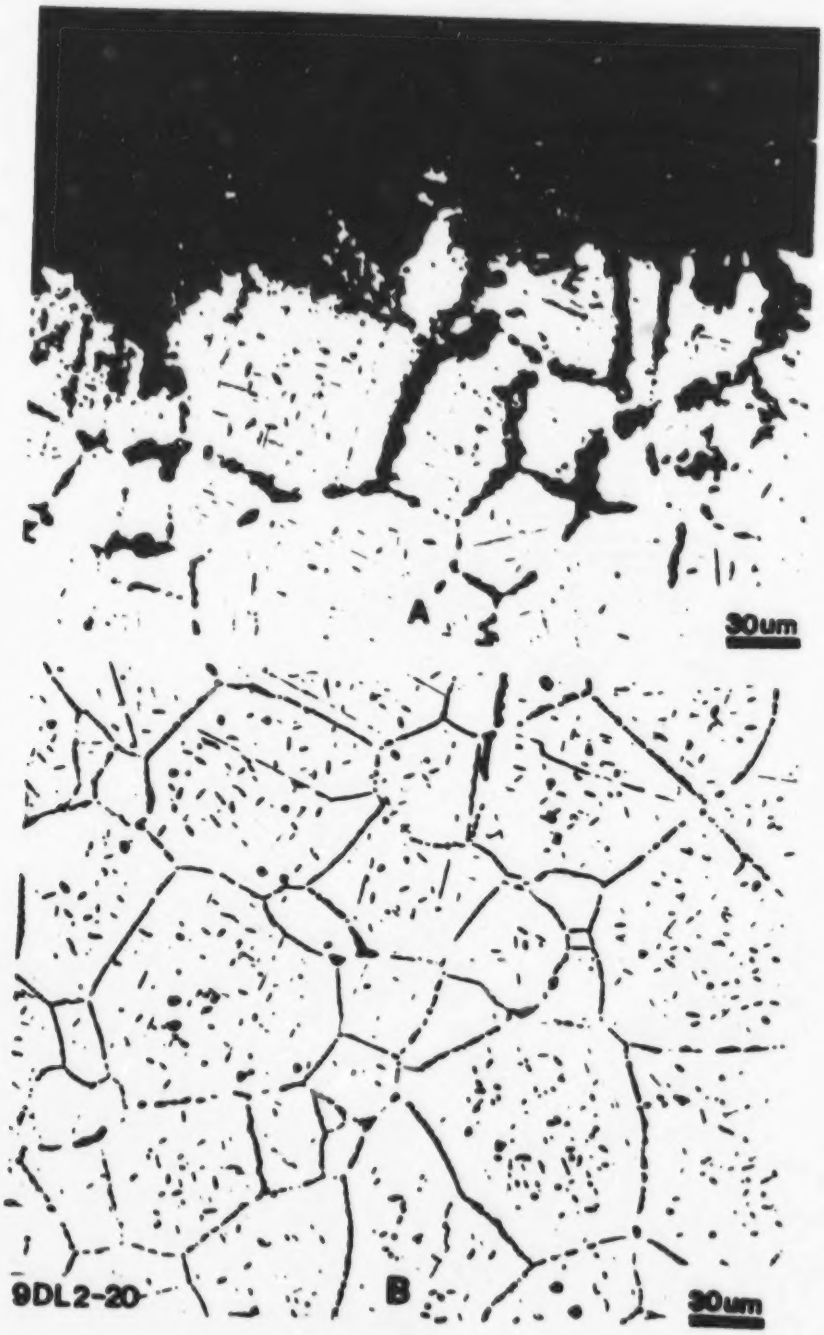

Fig. 19 - Type Incoloy 800H alloy, bottom of the ring, exposed at 850°C for 3000 h.

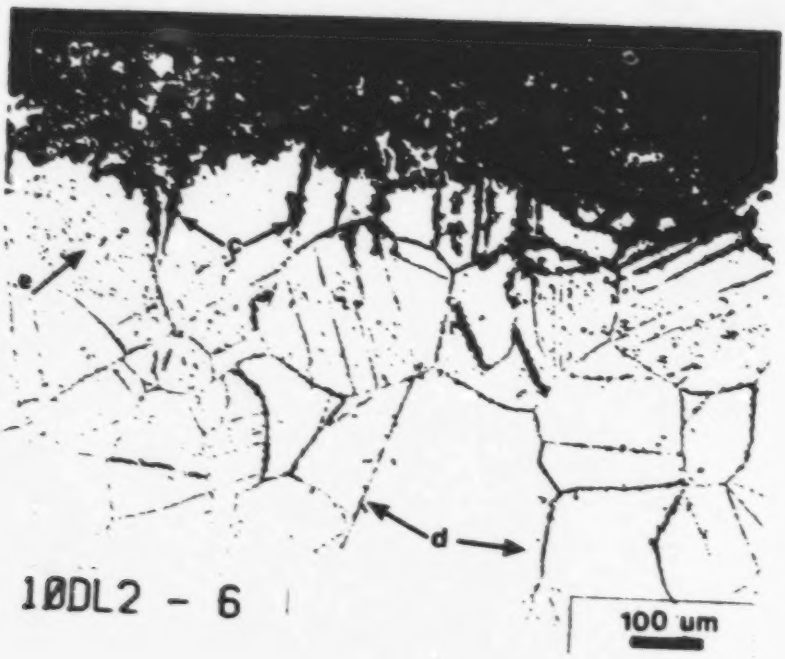


| Feature | Position | S | Ca | Cr | Mn | Fe | Ni | O |
|---|---|---|---|---|---|---|---|---|
| Scale | 19,a | 0.3-0.5 | -- | 59.8-62.4 | -- | 1.1 | 1.4-1.9 | 34.4-36.3 |
| outer region | | (0.3-0.4) | | (32.9-35.2) | | (0.6) | (0.7-0.9) | (63-65) |
| Scale | 19,b | 18 | -- | 61.4 | -- | -- | -- | 19.2 |
| inner region | | (18.9) | | (39.8) | | | | (40.5) |
| Intrusions | 19,c | 0.2-2.9 | -- | 51.8-58.3 | -- | 1-1.6 | 1.2-2.2 | 39.1-42.0 |
| | | (0.1-2.4) | | (26.4-31) | | (0.5-0.8) | (0.6-1.0) | 67.7-69.7 |
| Intergranular | 19,d | 5.2-5.5 | -- | 37.9-42.4 | -- | 5.4-8.6 | 3.7-6.0 | 42.0 |
| Precipitates | | (4.3-4.9) | | (19.3-21.4) | | (2.6-4.1) | (1.7-2.7) | (69.4) |
| Intragranular | 19,e | 37.5 | -- | 51.7 | 2.3 | 1.9 | 2.0 | 4.7 |
| Precipitates | | (45.6) | | (38.8) | (1.6) | (1.3) | (1.3) | (11.4) |

Fig. 20 - Deeply-etched cross-section of an Incoloy 800H sample showing the intergranular and twin-boundary precipitates.

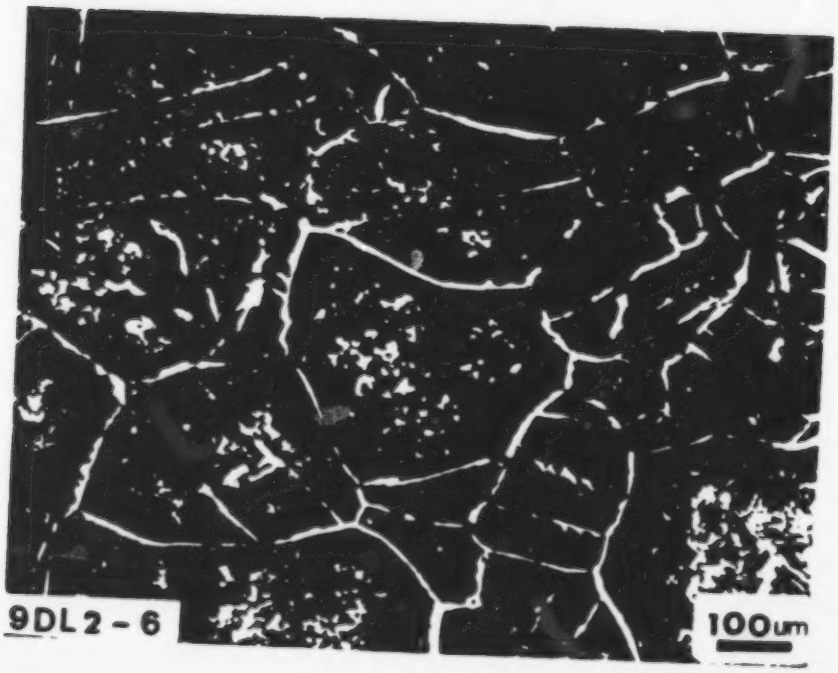

Fig. 21 - Type Incoloy 800H alloy, bottom of the ring, exposed at 850°C for 3000 h.

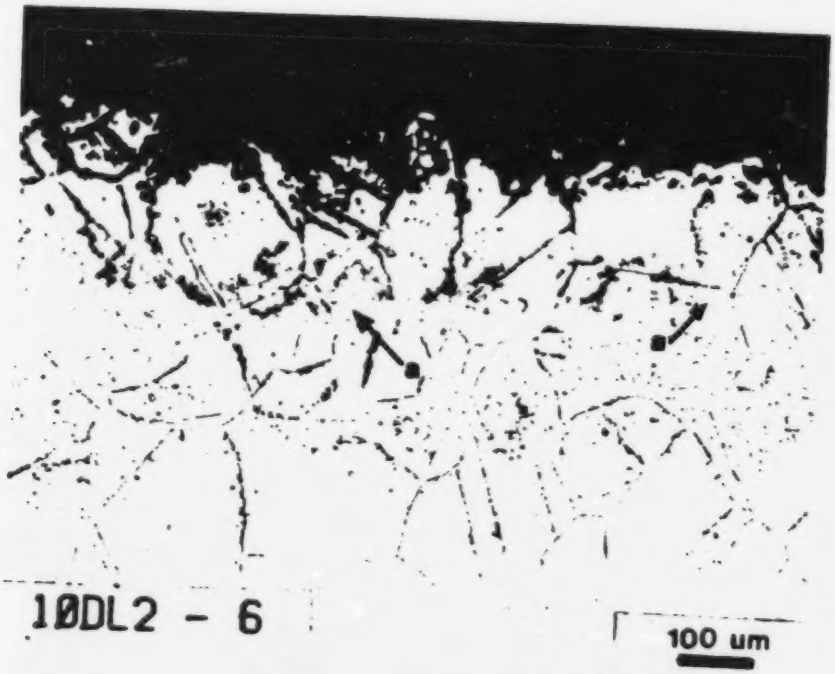


| Feature | Position | S | Ca | Cr | Mn | Fe | Ni | O |
|---|---|---|---|---|---|---|---|---|
| Irregular Phase | 21,a | 31.7-40.4 (31.3-50.3) | -- | 46.0-55.5 (28-42.9) | 1.8-2.2 (1.1-1.5) | -- | -- | 2.1-19.9 (5.2-39.3) |

Fig. 22 - Electron images and corresponding X-ray maps for the patchy phase formed in an Incoloy 800H (same sample as Fig. 21).

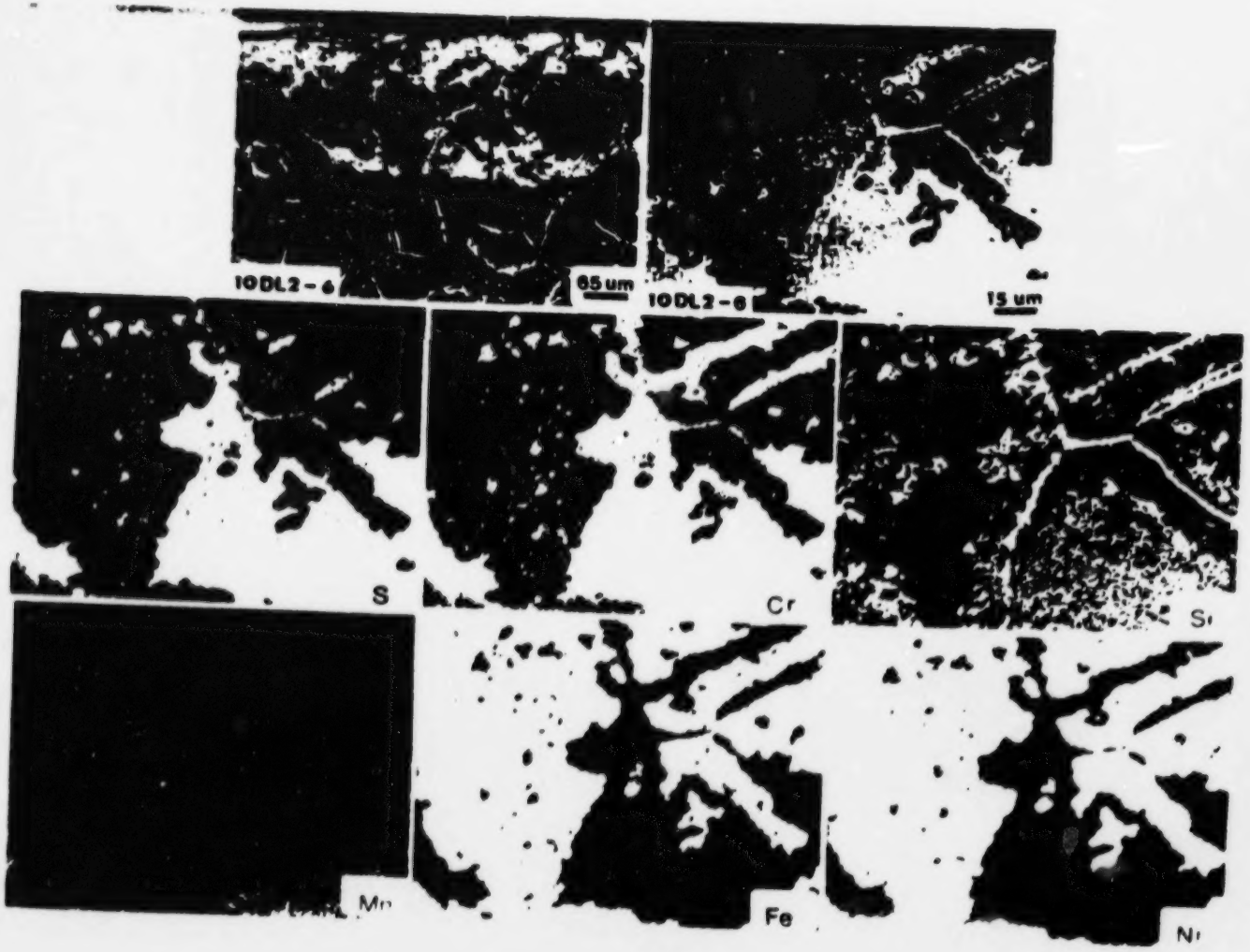

Fig. 23 - Micro-photograph of a region neighbouring the perforation found in an Incoloy sample which was exposed at 850°C for 1000 h.

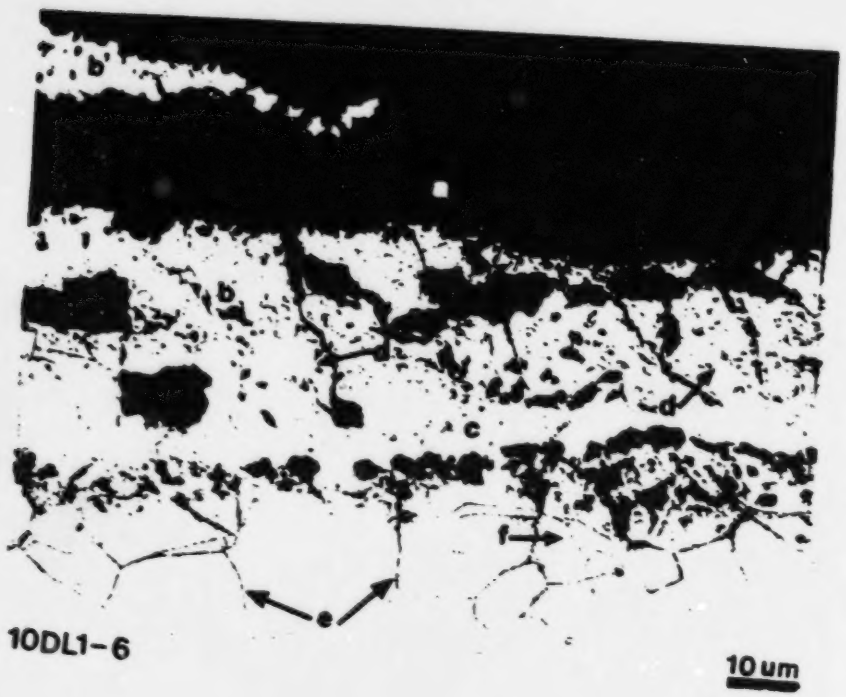


| Feature | Position | S | Ca | Cr | Mn | Fe | Ni | O |
|---|---|---|---|---|---|---|---|---|
| Outer layer | 23,a | 0.4-0.9 (0.4-0.7) | -- | 49.8-62.4 (24.8-34.5) | -- | 0.3-1.0 (0.1-0.5) | 1-3.3 0.5-1.5 | 35.8-44.8 (64.4-72.4) |
| Intermediate layer | 23,b | 11.9-30.2 (18.7-39.1) | -- | -- | -- | 28.6 (23) | 35.4-57.2 (25-49) | 2-5.5 (6.3-14.4) |
| | 23,b' | 27.7-29.1 (31.3-37.3) | -- | 0.6 (0.5) | -- | 27.5-30.3 (18-22.3) | 29.8-33.8 (18.4-23.7) | 6.3-14.0 (16.2-31.6) |
| Inner layer | 23,c | 36.6 (44.2) | -- | 13.8 (10.3) | 0.7 (0.5) | 29.7 (20.6) | 12.4 (8.2) | 6.7 (16.2) |
| Precipitates in intermediate layer | 23,d | -- | -- | -- | -- | 29.5-34.5 (28.2-33.5) | 57.2-66.4 (58.5-60.3) | 2.3-3.0 (7.8-10) |
| Intergranular Precipitates | 23,e | 5.3-17.3 (4.6-15.8) | -- | 20.8-41.4 (11.7-24.2) | 0.3-1.5 (0.1-0.7) | 8.1-15.2 (4.1-8.0) | 6.2-15.4 (2.6-7.7) | 29.7-47.7 (56.4-73.7) |
| Intragranular Precipitates | 23,f | 19.3-28.5 (21.6-32.4) | -- | 11.6-19.8 (8.6-13.2) | 0.3-0.7 (0.2-0.4) | 21.9-30.4 (13.6-19.8) | (12.7-30.7) (7.9-20.2) | 12.5-18.6 (28.9-40.1) |

Fig. 24 - Electron image and X-ray maps for the sample shown in Fig. 23.